Understanding triggering mechanisms for critical heat flux in pool boiling based on direct numerical simulations

Understanding Triggering Mechanism for Critical Heat Flux in Pool Boiling Based on Direct Numerical Simulations

Shuai Gong[1, 2, ǂ], Lenan Zhang[2, ǂ], Ping Cheng[1, *], Evelyn N. Wang[2, *]

1. School of Mechanical Engineering, Shanghai Jiao Tong University, Shanghai 200240, China

2. Department of Mechanical Engineering, Massachusetts Institute of Technology, Cambridge, Massachusetts 02139, USA

Abstract

Boiling is a ubiquitous process in many applications including power generation, desalination, and high-heat flux electronic cooling. At the same time, boiling is a complicated physical process involving hydrodynamics and interfacial heat and mass transfer on multiple scales. One of the key limiting factors of boiling is the critical heat flux (CHF), beyond which a vapor blanket forms on the heating surface and catastrophic device burnout occurs. Yet, detailed understanding of the mechanism that triggers CHF remains elusive. In this paper, we elucidate the CHF mechanism by studying the evolution of wet/dry region on the heater surface using lattice Boltzmann simulations. We incorporate the equation of state for real gases in the liquid-vapor phase change model for direct numerical simulation of the CHF phenomenon. The results of this framework clarify the difference between the triggering mechanism of CHF and film boiling by analyzing the pool boiling curve. We demonstrate that the heat flux of the wet region on the heater surface increases while the wet area fraction decreases with superheat, leading to the CHF. We show that a vapor recoil force due to the interfacial heat and mass transfer plays an important role for the evolution of wet area fraction and therefore contributes to the occurrence of a second transition regime and CHF. Compared with previous CHF models which treat CHF as an isolated point on the boiling curve, this work elucidates the triggering mechanism of CHF from a perspective of the dynamic evolution of the wet/dry region with increasing superheat, which could potentially serve as a guideline for future CHF enhancement designs.

Key words: critical heat flux, liquid-vapor interface, boiling curve, bubble, interfacial heat and mass transfer

---

ǂ Author Contributions: S. Gong and L. Zhang contributed equally to this work.

* Corresponding authors: pingcheng@sjtu.edu.cn (P. Cheng), enwang@mit.edu (E.N. Wang)

Introduction

Most of the world's electricity is generated from steam cycles [1], in which boiling is a central process. Boiling is also widely used in desalination, electronic cooling, chemical processing and nuclear reactor safety [2]. As one of the most efficient heat transfer modes, boiling heat transfer has been an intensively studied phenomenon in the thermal sciences over the past 80 years. In particular, critical heat flux (CHF), which is of importance to both the safe operation and efficiency of a boiling equipment, has attracted considerable research interest [3-5]. Although a significant number of efforts have been carried out during the past several decades, fundamental understanding of the mechanism that triggers CHF remains limited due to the chaotic nature, strong coupling of heat and mass transfer, complex hydrodynamics and interfacial phenomena, as well as the multiscale behavior of boiling.

Many CHF models or mechanisms have been proposed since the 1940s [6-12]. In particular, the hydrodynamic instability model [7] and the macrolayer dryout model [8] have attracted a great deal of attention. The hydrodynamic instability model assumes that CHF occurs when the interface of the vapor columns leaving the surface becomes Helmholtz unstable, which would cause the coalescence of vapor columns and formation of a vapor blanket over the heating surface [7]. The macrolayer dryout model postulates that there exists a big mushroom bubble due to the coalescence of many vapor stems at numerous nucleation sites. A liquid layer, known as the macrolayer, is trapped under the mushroom bubble. CHF is triggered when the liquid macrolayer dries out before the departure of the mushroom bubble [8]. Although these models can give reasonable prediction to the value of CHF for flat surfaces, they are not consistent with many recent experimental findings [13, 14], and no consensus has been reached on the triggering mechanism of CHF.

Fig. 1 shows a schematic of boiling curves under both controlled temperature (1-2-3-4-5-6-7) and controlled heat flux (1-2-3-6-7) conditions. Point 3 is the CHF for both conditions, and the CHF mechanism should describe the transition from Point 2 to 3. Note the transition boiling regime between 3-4-5 on the controlled temperature boiling curve indicates that the heating surface is still partially covered by liquid after the CHF [2]. For this reason, a vapor blanket formation due to coalescence of vapor columns [7], dryout of macrolayer [8], and spreading of vapor under the force due to exiting vapor momentum [10] as described by various models [7, 8, 10] elucidate the

triggering mechanism of film boiling (from Point 3 to 6) instead of CHF (from Point 2 to 3). The reason that they are treated as the mechanism of CHF is because most boiling experiments were performed by changing the heat flux rather than superheat. The transition from Point 3 to 6 occurs in an instant and it is hard to distinguish the CHF (Point 3) from the film boiling (Point 6) in a controlled heat flux boiling experiment.

Therefore, a rational CHF triggering mechanism should relate the CHF to the high heat flux nucleate boiling regime before it occurs (*i.e.,* Point 2-3). Due to the intrinsic complexities associated with the CHF phenomenon, direct numerical simulation of CHF is limited [15, 16]. Recently, Sato and Niceno [16] successfully simulated pool boiling CHF phenomenon using an interface tracking method by prescribing a nucleation-site model *a priori*. In this work, we perform direct numerical simulation of pool boiling under a controlled wall temperature condition using the lattice Boltzmann method. We obtain direct numerical simulations of pool boiling curves including CHF by incorporating the equation of state for real gases in our model, which enables liquid-vapor phase change determined by the thermodynamic relations governed by the equation of state. As a result, there is no need to explicitly track the liquid/vapor interface and prescribe a nucleation-site model in our numerical approach, and the dynamic evolution of the nucleate boiling regime (1-2-3), CHF, and transition boiling (3-4-5) regime is well-resolved to elucidate the CHF triggering mechanism. We show that the surface covered by liquid, defined as the wet region, dominates the nucleate boiling heat transfer regime. With the increase of wall superheat, the heat flux from the wet region increases while the area of the wet region decreases, leading to a local maximum point for the overall heat flux, *i.e.*, CHF. We further demonstrate that the sharp decrease of wet area fraction that triggers the second transition regime and CHF can be attributed to the change of apparent contact angle, which is driven by a vapor recoil force [17-19] due to the high interfacial heat/mass flux near the three-phase contact line. The present study elucidates that CHF is a natural outcome of nucleate boiling due to the opposite trend of the wet region heat flux and area fraction. More importantly, from this perspective, the substrate effects (*i.e.*, the surface roughness, wettability and porosity) on CHF, which had not been considered by existing prevailing CHF models [7, 8] but experimentally demonstrated in many past works [3-5, 20], can also be properly addressed in the future.

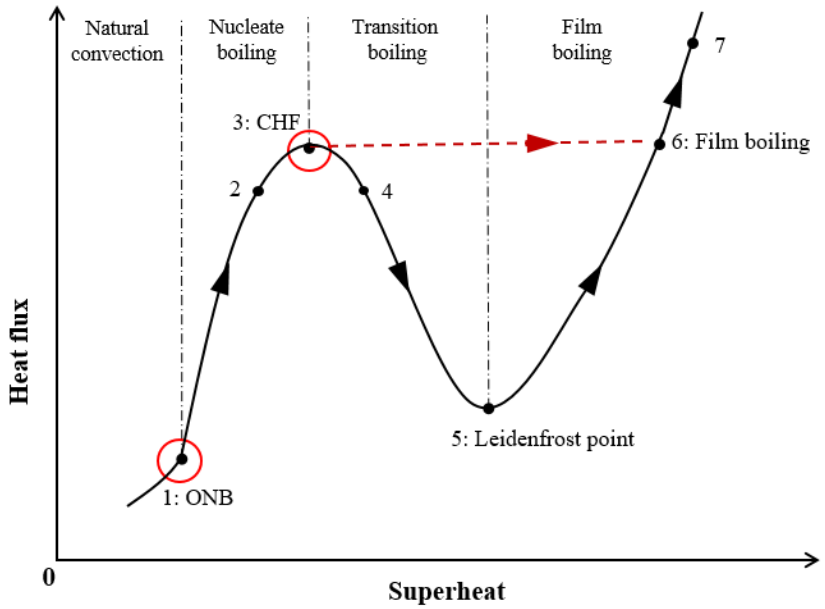

Fig. 1. Schematic of boiling curves under controlled temperature condition (1-2-3-4-5-6-7) and controlled heat flux condition (1-2-3-6-7). In the transition boiling regime (3-4-5) after CHF (Point 3), the heating surface is still not fully covered by the vapor film. The phenomenological models which describe how a vapor blanket forms [7, 10] or macrolayer dryout occurs [8] actually elucidate the triggering of film boiling (from Point 3 to 6) instead of the triggering of CHF (from Point 2 to 3).

Results and discussion

We performed direct numerical simulations of pool boiling process under controlled wall temperature condition using the lattice Boltzmann method (LBM) and incorporating the equation of state (EOS) for a real gas into the phase change model (See Sections S1-S3 of Supplementary Information for the numerical method). Fig. 2 shows the simulated saturated pool boiling curve from the nucleate boiling regime to film boiling regime through the CHF and transition boiling regime, where *Ja* is the dimensionless superheat defined as,

$$Ja = c_{p,l}(T_w - T_{sat}) / h_{fg} \tag{1}$$

with T_w being the space- and time- averaged wall temperature over the heating surface, $c_{p,l}$ the specific heat for the liquid and h_{fg} the specific latent heat (See Section S6 of Supplementary Information for the derivation of the specific latent heat for any given equation of state). The simulated saturated pool boiling curve as shown in Fig. 2 has the same feature with the classical

Nukiyama boiling curve [21]. To validate our approach, two representative points on the boiling curve, *i.e.*, the CHF (Point C) and Leidenfrost point (Point E), were compared with existing theoretical models [7, 10, 22] and good agreement was achieved. The simulated film boiling heat transfer rate also agrees well with the Berenson model [22] and Klimenko model [23]. Details about our model validation and comparison with classical theories can be found in Sections S7-S8 of the Supplementary Information.

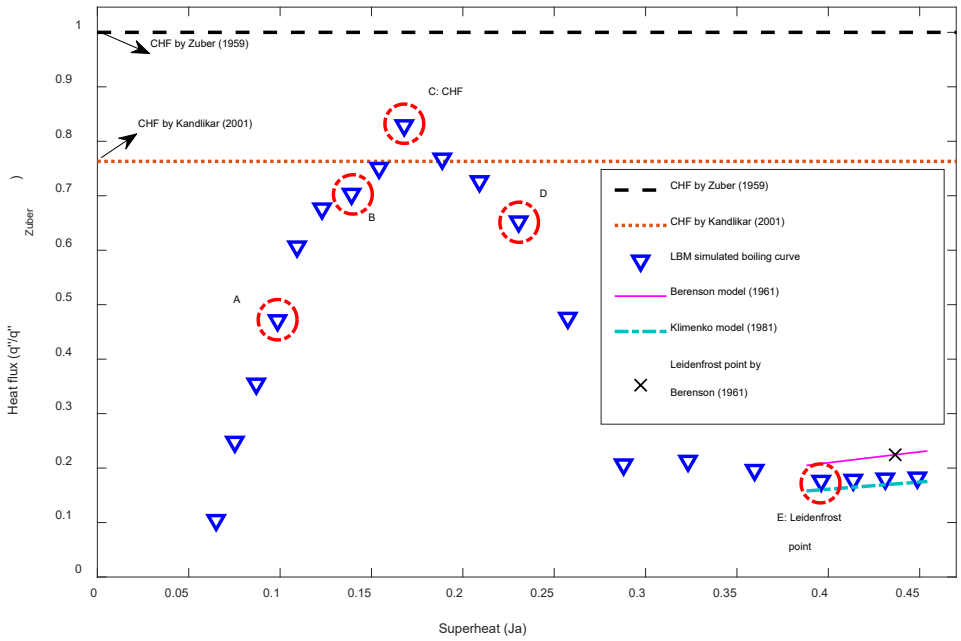

Fig. 2. Saturated pool boiling curve under controlled temperature condition on a hydrophilic heating surface using LBM simulations. Bubble nucleation and liquid-vapor phase change automatically occur in the simulation due to the fact that the equation of state for real gas has been incorporated into the model. Different boiling regimes, *i.e.*, the nucleate boiling, CHF, transition boiling, and film boiling regime were reproduced by our proposed LBM phase change model. Point A is in the isolated regime of the nucleate boiling, Point B is the starting point for the second transition regime [24] of nucleate boiling, Point C is the CHF, Point D is a representative point during the transition boiling and Point E is the Leidenfrost point. The simulated CHF value, Leidenfrost point and film boiling heat transfer were compared with classical models [7, 10, 22, 23], showing good agreement .

We analyzed four representative states on the boiling curve shown in Fig. 2, where Point A is in the nucleate boiling regime, Point C is at the CHF, Point D is in the transition boiling regime and

Point E is the Leidenfrost point in the film boiling regime. Fig. 3 shows images of boiling patterns at different instants obtained from DNS. At Point A, bubbles on the heating surface are isolated. At CHF (Point C), however, strong interactions between adjacent nucleation sites and unstable boiling patterns are observed. In the transition boiling regime (Point D), intermittent partial dryout occurs on the heating surface and the dry area fraction becomes larger than the CHF. At the Leidenfrost point (Point E), the heating surface is completely covered by the vapor film and bubbles are released periodically at the peak of a Taylor instability wave.

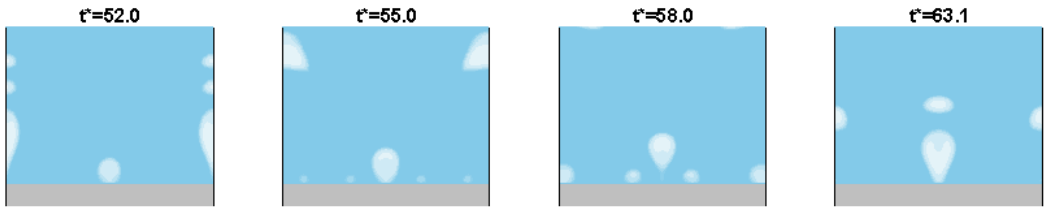

(a) Nucleate boiling regime (Point A in Fig. 2)

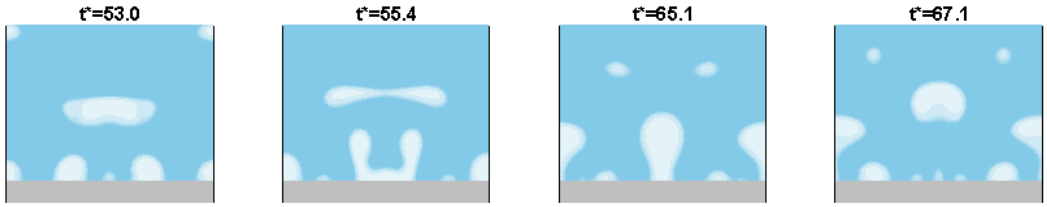

(b) CHF (Point C in Fig. 2)

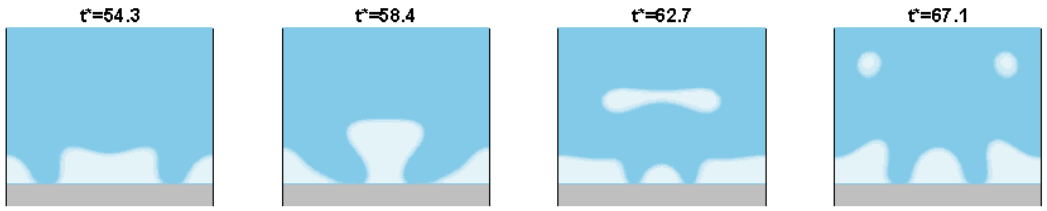

(c) Transition boiling regime (Point D in Fig. 2)

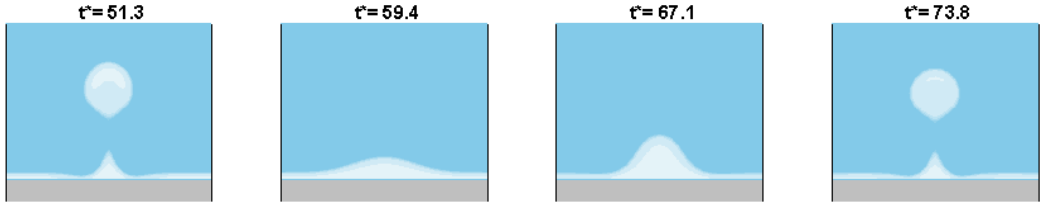

(d) Film boiling regime (Point E in Fig. 2)

Fig. 3. Images of the boiling pattern at different instants in the (a) nucleate boiling regime, (b) CHF, (c) transition boiling regime and (d) film boiling regime with LBM simulation (Dark grey: heater;

Light blue: liquid; Light grey: vapor bubble). Isolated bubble growth and departure are observed in the nucleate boiling regime at Point A on the boiling curve (Fig. 2). Strong bubble interactions are shown at CHF and the surface exhibits intermittent partial dryout in the transition boiling regime. The heating surface is completely covered by the vapor film at the Leidenfrost point, and bubble departure occurs at the peak of the Taylor instability wave.

The boiling patterns shown in Fig. 3 indicate the evolution of dry/wet area fraction plays a key role in the transition between boiling regimes. To elucidate the transition mechanism from nucleate boiling to CHF, the total heat flux is decomposed into two components,

$$q''_{tot} = q''_{wet}\frac{A_{wet}}{A} + q''_{dry}\frac{A_{dry}}{A} \tag{2}$$

where q''_{wet} and q''_{dry} are the space- and time-averaged heat flux on the wet region and dry region of the heating surface, A_{wet} and A_{dry} are the time-averaged area of the wet region and dry region, $q''_{wet}A_{wet}/A$ and $q''_{dry}A_{dry}/A$ represent the contribution of the wet region and dry region to the total heat transfer, respectively. Fig. 4 shows the wet area fraction (A_{wet}/A), dry area fraction (A_{dry}/A), q''_{wet}, q''_{dry}, wet region heat flux contribution ($q''_{wet}A_{wet}/A$) and dry region heat flux contribution ($q''_{dry}A_{dry}/A$) as a function of wall superheat. Fig. 4(a) shows that the wet area fraction decreases while the dry area fraction increases with the superheat. At the same time, Fig. 4(b) shows that q''_{wet} increases monotonically with the superheat. Fig. 4(c) demonstrates that the contribution of the wet region ($q''_{wet}A_{wet}/A$) is the dominant heat flux component in the nucleate boiling regime including the CHF. Since q''_{wet} increases while A_{wet}/A decreases simultaneously with the increasing superheat, it is expected that their product, *i.e.*, $q''_{wet}A_{wet}/A$, has a local maximum, which corresponds to the CHF as shown in Fig. 4(c). Note that q''_{wet} can be decomposed further to the contribution from microlayer evaporation [25], microconvection [26, 27], transient conduction [28, 29] and natural convection [27], but the relative contribution from these sub-mechanisms is out of the scope of this work.

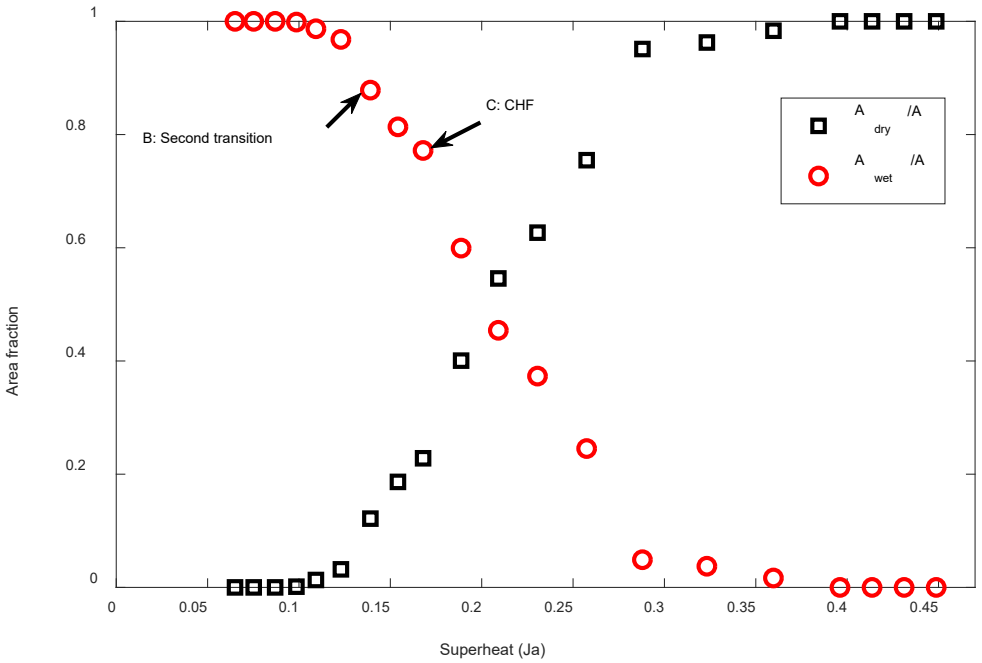
Area fraction
Superheat (Ja)
B: Second transition
C: CHF
A /A
dry
A /A
wet

(a)

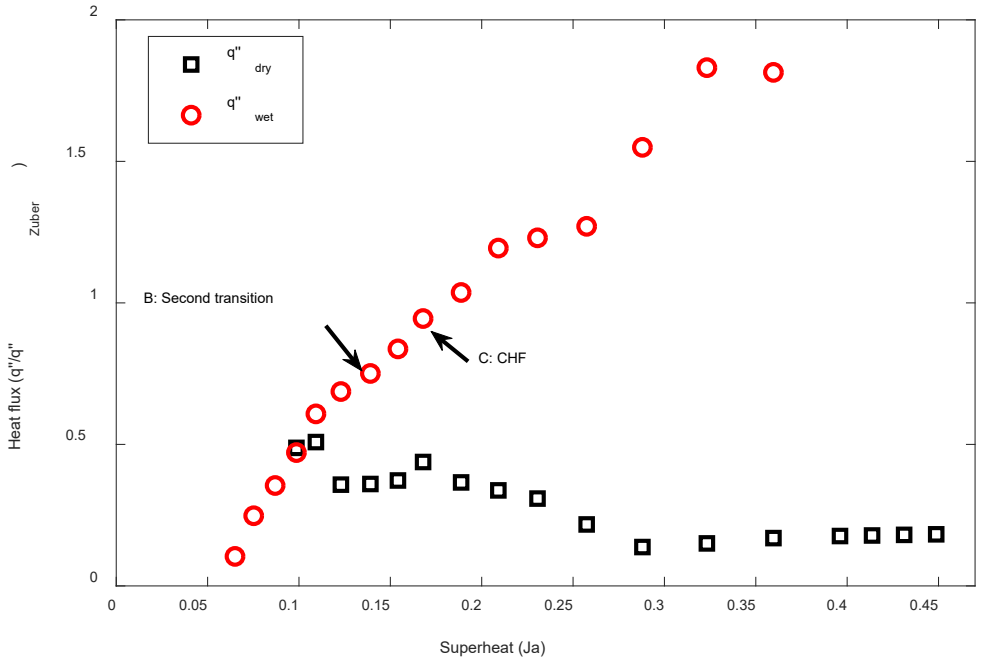
Heat flux (q"/q"
Zuber
)
Superheat (Ja)
B: Second transition
C: CHF
q"
dry
q"
wet

(b)

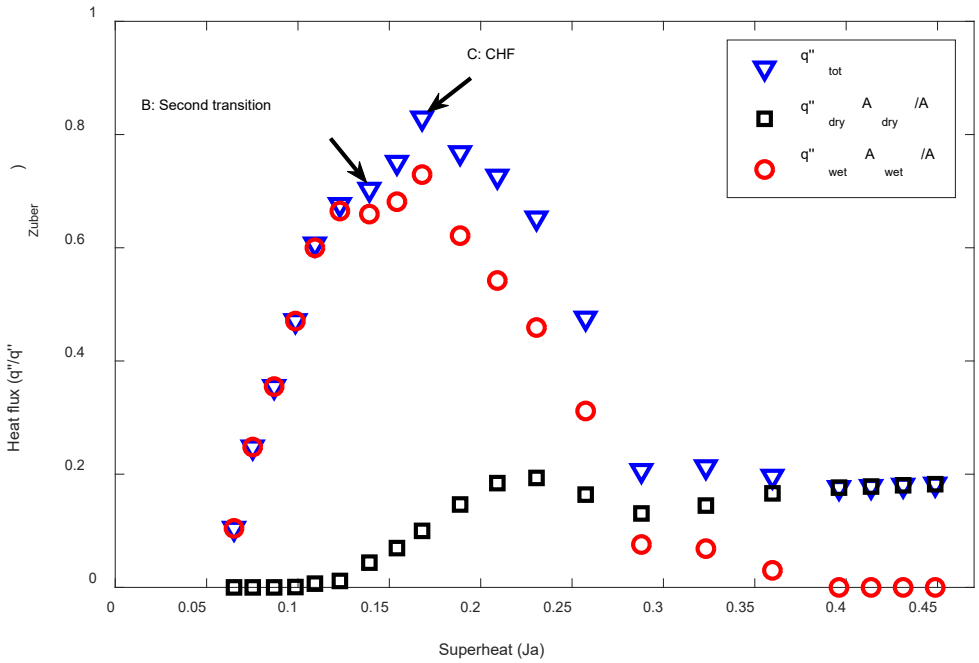

(c)

Fig. 4. Simulation results of (a) dry area fraction and wet area fraction, (b) dry region heat flux and wet region heat flux, and (c) dry region heat transfer contribution and wet region heat transfer contribution as a function of superheat. Heat transfer from the wet region dominates the total heat flux in the nucleate boiling regime and CHF. The wet area fraction decreases while the wet region heat flux increases as the increase of superheat, which leads to a local maximum, *i.e.*, the CHF in their product.

Fig. 4 demonstrates that CHF is a natural outcome during the evolution of the wet region heat transfer with respect to the increase of wall superheat. However, it is still not clear why the wet area fraction drops sharply close to the CHF as shown in Fig. 4(a). To explain this, we compared the boiling patterns, local temperature and local heat flux distributions on the heating surface (*i.e.*, at the fluid-heater interface) for Point A (nucleate boiling regime) and Point C (CHF) in Fig. 5, where T' is the dimensionless temperature defined as $T' = (T - T_{sat})/(T_b - T_{sat})$, with T_b being the temperature at the bottom of the heater. In the nucleate boiling regime (Fig. 5(a)), bubbles are of spherical shape, with an apparent contact angle less than 90° for a hydrophilic heating surface used in the simulation. Due to microlayer evaporation and the lateral heat conduction from the center of the bubble to the three-phase contact line, a cold spot (where the temperature is lower than that of the surrounding

region) with a high local heat flux was observed at the bubble base region. Fig. 5(b) shows that at CHF, large hot spots with very low local heat flux were observed at the bubble base due to the depletion of microlayer. Since the static contact angle used in the simulation is 41° (see Section S5 of Supplementary Information), Fig. 5(b) shows that there is an obvious increase of the apparent contact angle at CHF. In particular, for the merged bubble at the center of the heater which is undergoing a rewetting process by the surrounding liquid, its apparent contact angle is even larger than 90°, implying that there is a residual bubble after bubble departure. That is to say, the waiting period after bubble departure disappears and this region becomes a permanent dry region. The changes of bubble morphology and apparent contact angle have both spatial and temporal effects on the evolution of the wet area fraction. Specifically, the increase of bubble size and apparent contact angle results in a larger bubble base area and contributes to the decrease of the wet area fraction after a spatial average. Meanwhile, the permanent dry region and the disappearance of the bubble waiting period in the ebullition cycle lead to the decrease of the wet area fraction in the temporal domain.

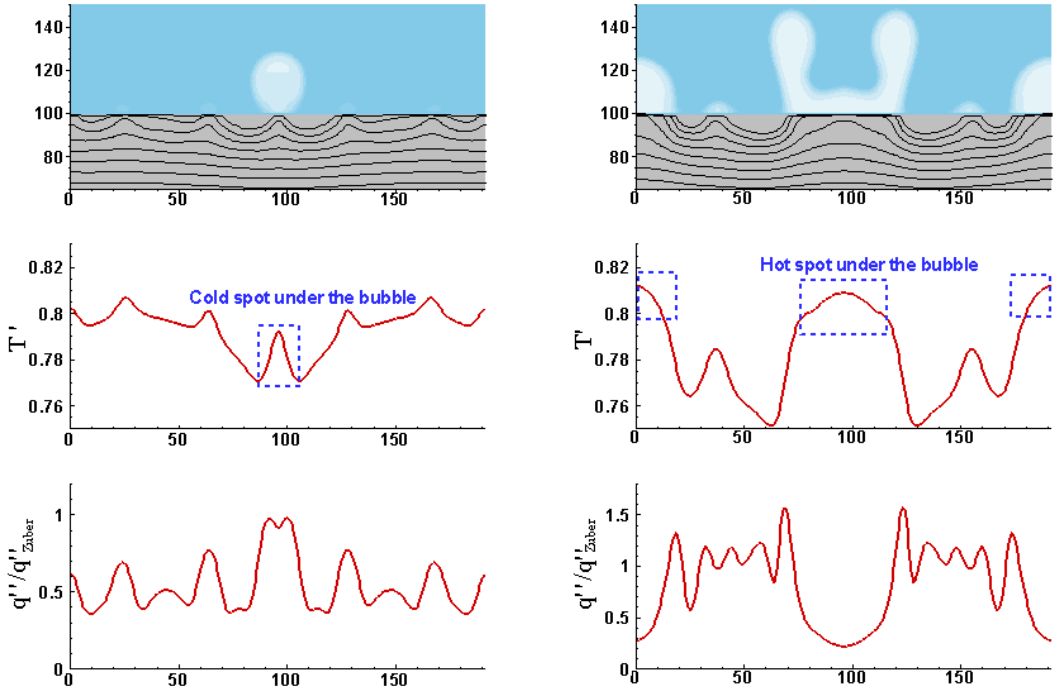

(a) Nucleate boiling at Point A (b) CHF at Point C

Fig. 5. Simulation results of boiling pattern, local temperature and local heat flux distributions on the heating surface for (a) nucleate boiling regime at Point A and (b) CHF at Point C. A cold spot at the bubble base was observed during the nucleate boiling due to the microlayer evaporation, while

it becomes a hot spot at the CHF due to the depletion of microlayer. The changes of bubble morphology and apparent contact angle drive the expansion of the dry area, which contributes to the occurrence of CHF.

To further explain the increase of apparent contact angle with heat flux, we considered the heat and mass transfer through the liquid-vapor interface. Since the magnitude of vapor velocity $\boldsymbol{u}_v$ is much larger than that of the liquid velocity $\boldsymbol{u}_l$, the momentum carried by the vapor flux is stronger. This result leads to a vapor recoil force acting on the liquid-vapor interface (Fig. 6(a)). Applying the conservation of mass and momentum at the three-phase contact line of the bubble (Section S9 of Supplementary Information for detailed derivations), we show that the relationship between the apparent contact angle θ and the heat flux at the three-phase contact line q''_{CL} can be expressed as,

$$\left(\frac{q''_{CL}}{h_{fg}}\right)^2\left(\frac{1}{\rho_v}-\frac{1}{\rho_l}\right)\sin\theta = 2\sigma\kappa(\cos\theta_0-\cos\theta) \tag{3}$$

where θ_0 is the static contact angle, σ is the surface tension, κ is the mean curvature of the interface, ρ_v and ρ_l are the density of the vapor and liquid phase respectively. Eq. (3) is plotted as a solid curve in Fig. 6(b) showing the apparent contact angle as a function of the heat flux at the contact line. The apparent contact angle θ can be significantly changed especially at high heat flux. In addition, the increase of apparent contact angle obtained from LBM simulation can be reasonably predicted by Eq. (3) (Section S9 of Supplementary Information for details). When the apparent contact angle is larger than 90^o, a permanent dry spot forms after the vapor neck pinches off (inset of Fig. 6(b)). It is also interesting to note that simulation results suggest that a second transition point (Point B on Fig. 2 and Fig. 4(c)) [24], where the slope of the boiling curve begins to decrease and heat transfer coefficient reaches a maximum, corresponds to the apparent contact angle of 90^o as shown in Fig. 6(b). This result provides evidence that the formation of permanent dry spots and the resultant sharp decrease of wet area fraction (Fig. 4 (a)) induce the second transition point in the nucleate boiling regime and accelerate the occurrence of CHF, which is consistent with experimental findings by Gaertner [24].

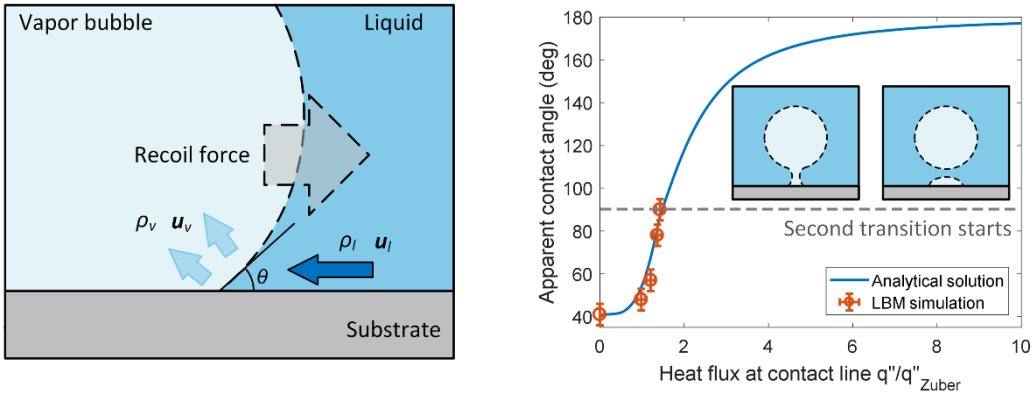

(a) (b)

Fig. 6. Relationship between the apparent contact angle and heat flux close to the three-phase contact line. (a) Schematic of mass and momentum conservation at the contact line. At the liquid-vapor interface, the magnitude of vapor velocity is larger than that of the liquid due to the conservation of mass, which leads to stronger momentum carried by the vapor flux. A vapor recoil force acts on the liquid-vapor interface to balance the momentum, which increases the apparent contact angle. (b) Apparent contact angle as a function of the heat flux at the contact line. The change of apparent contact angle observed in the LBM simulation was compared with the analytical solution given by Eq. (3), showing good agreement. The grey-dash line indicates 90° contact angle after which permanent dry spot forms and second transition regime starts. Inset: formation of the permanent dry spot due to the increase of apparent contact angle. The error bar shown in the LBM results indicates the uncertainty of the apparent angle and contact line heat flux, which arises from temporal and spatial fluctuations during boiling.

Conclusion

In this paper, we have shown physical insights on the triggering mechanism of critical heat flux (CHF) by using direct numerical simulations. We demonstrated that the heat transfer from the wet region dominates the overall heat transfer in the nucleate boiling regime up to the CHF. These numerical results suggested that CHF is a natural outcome due to the opposite trend of the heat flux and area fraction of the wet region with increasing wall superheat. Permanent dry spots form due to the increased apparent contact angle, which is driven by a vapor recoil force. We also show that the second transition point in the nucleate boiling regime corresponds to an increased apparent contact

angle of 90°. The vapor recoil force arises from the interfacial heat/mass transfer near the three-phase contact line, which accelerates the decrease of wet area fraction and contributes to the occurrence of second transition regime and CHF. This work not only provides insights into the triggering mechanism for CHF based on the dynamic evolution of the wet/dry region, but could serve as a tool to guide the design for CHF enhancement.

Supplementary material

The Supplementary material including Numerical model, Computation setup, Conjugate heat transfer treatment at fluid-solid interface, Determination of surface tension, Determination of contact angle, Derivation of the specific latent heat for any given equation of state, Boiling curve, Model validation and Analytical model for the effect of contact line heat flux on the apparent contact angle, is available at:

Acknowledgements

S. Gong would like to acknowledge the support from National Natural Science Foundation of China (No. 51706135), National Science and Technology Major Project (No. 2018ZX06002004), Foundation for Innovative Research Groups of National Natural Science Foundation of China (No. 51521004), and International Postdoctoral Exchange Fellowship Program (No. 20170049) by China Postdoctoral Council. L. Zhang would like to acknowledge the support from the Singapore-MIT Alliance for Research and Technology (SMART) LEES Program.

References

[1] I.E. Agency, Key World Energy Statistics 2016, 2016.
[2] V.P. Carey, Liquid-Vapor Phase-Change Phenomena: An Introduction To The Thermophysics Of Vaporization And Condensation Processes In Heat Transfer Equipment, Taylor & Francis Group, New York, 2008.
[3] D.I. Shim, G. Choi, N. Lee, T. Kim, B.S. Kim, H.H. Cho, Enhancement of Pool Boiling Heat Transfer Using Aligned Silicon Nanowire Arrays, Acs Appl Mater Inter, 9(20) (2017) 17595-17602.
[4] H.J. Cho, D.J. Preston, Y. Zhu, E.N. Wang, Nanoengineered materials for liquid–vapour phase-change heat transfer, Nature Reviews Materials, 2(2) (2016) 1-17.
[5] K.-H. Chu, Y. Soo Joung, R. Enright, C.R. Buie, E.N. Wang, Hierarchically structured surfaces for boiling critical heat flux enhancement, Applied Physics Letters, 102(15) (2013) 151602.
[6] S. Kutateladze, On the transition to film boiling under natural convection, Kotloturbostroenie, 3

(1948) 10-12.
[7] N. Zuber, Hydrodynamic aspects of boiling heat transfer, Univ. of California, Los Angeles, CA (United States), 1959.
[8] Y. Haramura, Y. Katto, A new hydrodynamic model of critical heat flux, applicable widely to both pool and forced convection boiling on submerged bodies in saturated liquids, Int J Heat Mass Tran, 26(3) (1983) 389-399.
[9] V.S. Nikolayev, D.A. Beysens, Boiling crisis and non-equilibrium drying transition, Europhysics Letters (EPL), 47(3) (1999) 345-351.
[10] S.G. Kandlikar, A theoretical model to predict pool boiling CHF incorporating effects of contact angle and orientation, J. Heat transfer, 123(6) (2001) 1071-1079.
[11] N.S. Dhillon, J. Buongiorno, K.K. Varanasi, Critical heat flux maxima during boiling crisis on textured surfaces, Nature communications, 6(1) (2015) 1-12.
[12] L. Zhang, J.H. Seong, M. Bucci, Percolative scale-free behavior in the boiling crisis, Physical review letters, 122(13) (2019) 134501.
[13] T. Theofanous, T.-N. Dinh, J. Tu, A. Dinh, The boiling crisis phenomenon: Part II: dryout dynamics and burnout, Experimental Thermal and Fluid Science, 26(6-7) (2002) 793-810.
[14] J. Jung, S.J. Kim, J. Kim, Observations of the critical heat flux process during pool boiling of FC-72, Journal of Heat Transfer, 136(4) (2014) 041501.
[15] M. Yazdani, T. Radcliff, M.C. Soteriou, A. Alahyari, A high-fidelity approach towards simulation of pool boiling, Physics of Fluids, 28 (2016) 012111.
[16] Y. Sato, B. Niceno, Pool boiling simulation using an interface tracking method: From nucleate boiling to film boiling regime through critical heat flux, Int J Heat Mass Tran, 125 (2018).
[17] H.J. Palmer, The hydrodynamic stability of rapidly evaporating liquids at reduced pressure, Journal of Fluid Mechanics, 75(3) (1976) 487-511.
[18] K. Sefiane, D. Benielli, A. Steinchen, A new mechanism for pool boiling crisis, recoil instability and contact angle influence, Colloids and Surfaces A: Physicochemical and Engineering Aspects, 142(2-3) (1998) 361-373.
[19] V. Nikolayev, D. Chatain, Y. Garrabos, D. Beysens, Experimental evidence of the vapor recoil mechanism in the boiling crisis, Physical review letters, 97(18) (2006) 184503.
[20] K.-H. Chu, R. Enright, E.N. Wang, Structured surfaces for enhanced pool boiling heat transfer, Applied Physics Letters, 100(24) (2012) 241603.
[21] S. Nukiyama, The maximum and minimum values of the heat Q transmitted from metal to boiling water under atmospheric pressure, International Journal of Heat and Mass Transfer, 9(12) (1966) 1419-1433.
[22] P.J. Berenson, Film boiling heat transfer from a horizontal surface, J. Heat Transfer, 83(3) (1961) 351-356.
[23] V. Klimenko, Film boiling on a horizontal plate—new correlation, Int J Heat Mass Tran, 24(1) (1981) 69-79.
[24] R.F. Gaertner, Photographic study of nucleate pool boiling on a horizontal surface, Journal of Heat Transfer, 87(1) (1965) 17-27.
[25] M. Cooper, A. Lloyd, The microlayer in nucleate pool boiling, International Journal of Heat and Mass Transfer, 12(8) (1969) 895-913.
[26] S. Moghaddam, K. Kiger, Physical mechanisms of heat transfer during single bubble nucleate boiling of FC-72 under saturation conditions-I. Experimental investigation, International Journal of

Heat and Mass Transfer, 52(5-6) (2009) 1284-1294.
[27] J. Kim, Review of nucleate pool boiling bubble heat transfer mechanisms, International Journal of Multiphase Flow, 35(12) (2009) 1067-1076.
[28] H. Chi-Yeh, P. Griffith, The mechanism of heat transfer in nucleate pool boiling—part II: the heat flux-temperature difference relation, International Journal of Heat and Mass Transfer, 8(6) (1965) 905-914.
[29] B. Mikic, W. Rohsenow, A new correlation of pool-boiling data including the effect of heating surface characteristics, Journal of Heat Transfer, 91(2) (1969) 245-250.